1-17-2004

Unstable Layers in the Mesopause Region Observed with Na Lidar During the Turbulent Oxygen Mixing Experiment (TOMEX) Campaign

Alan Z. Liu
Embry Riddle Aeronautical University - Daytona Beach, liuz2@erau.edu

Raymond G. Roble
National Center for Atmospheric Research

James H. Hecht
The Aerospace Corporation

Miguel F. Larsen
Clemson University

Chester S. Gardner
University of Illinois at Urbana-Champaign

Unstable layers in the mesopause region observed with Na lidar during the Turbulent Oxygen Mixing Experiment (TOMEX) campaign

Alan Z. Liu,[1] Raymond G. Roble,[2] James H. Hecht,[3] Miguel F. Larsen,[4] and Chester S. Gardner[1]

Received 18 October 2002; revised 14 October 2003; accepted 31 October 2003; published 17 January 2004.

[1] The Na wind/temperature lidar located at Starfire Optical Range near Albuquerque, New Mexico, provided real time measurements of wind, temperature, and Na density in the mesopause region during the TOMEX rocket campaign in October 2000. The state of the atmosphere in which the rocket was launched into was examined using the lidar measurements. Both convectively and dynamically unstable layers were observed at various times and altitudes during the night. The low convective stability region below 90 km was found to be associated with the diurnal tide. The unstable layers are the combined results of wave and tidal perturbations. Comparison with the thermosphere/ionosphere/mesopshere/electrodynamics general circulation model (TIME-GCM) simulation showed that the model can produce the general feature of the observed atmospheric structure (but with a much smaller diurnal amplitude in temperature), which likely leads to underestimate of instability and gravity wave effects. *INDEX TERMS:* 3332 Meteorology and Atmospheric Dynamics: Mesospheric dynamics; 3360 Meteorology and Atmospheric Dynamics: Remote sensing; 3379 Meteorology and Atmospheric Dynamics: Turbulence; 3384 Meteorology and Atmospheric Dynamics: Waves and tides; *KEYWORDS:* instability, lidar, TIME-GCM

Citation: Liu, A. Z., R. G. Roble, J. H. Hecht, M. F. Larsen, and C. S. Gardner (2004), Unstable layers in the mesopause region observed with Na lidar during the Turbulent Oxygen Mixing Experiment (TOMEX) campaign, *J. Geophys. Res.*, *109*, D02S02, doi:10.1029/2002JD003056.

1. Introduction

[2] The atmosphere in the mesosphere and lower thermosphere (MALT) region often experience convective and dynamic instabilities due to large fluctuations from atmospheric gravity waves and tides. These wave activities and the turbulence associated with the instabilities induce large vertical transport and enhance the strong mixing of atomic oxygen, which is involved in several key chemical processes that play a major role in determining the structure and energetics of MALT region. In October 2000, the TOMEX (Turbulence Oxygen Mixing Experiment) campaign was conducted in New Mexico to investigate the mixing of atomic oxygen and the atmospheric response to instability layers in the MALT region [*Hecht et al.*, 2004]. A rocket was launched from White Sands Missile Range (WSMR, 33.72°N, 106.74°W) at about 10 UT on 26 October 2000 (hereafter TOMEX night). A Na wind/temperature lidar located at Starfire Optical Range (SOR, 34.96°N, 106.46°W) about 140 km north of WSMR probed the atmosphere region near the rocket trajectory above WSMR and measured winds and temperatures simultaneously. The measurement was displayed in real time during the campaign to provides guidance for the rocket launch. In this study, the lidar measurements were analyzed to examine the state of the atmosphere, and in particular its instability properties before, during and after the rocket launch.

[3] The Na lidar coupled with the large 3.5 m astronomical telescope at SOR can make temperature and wind measurements at high vertical and temporal resolution in the MALT region. The uncertainty of the SOR data is small enough for calculating the instability parameters N^2 (buoyancy frequency squared) and *Ri* (Richardson number) with good confidence as demonstrated in the work of *Zhao et al.* [2003]. Using the lidar data from SOR and Urbana Atmospheric Observatory (UAO, 40°N, 88°W), *Gardner et al.* [2002] showed that convective instability and gravity wave breaking most likely occur in the region between 80 and 90 km where the mean temperature has a large lapse rate and the N^2 is small. The instability probabilities and their altitudes vary with season and also during a night, as a result of varying mesopause altitude and tidal activities [*Gardner et al.*, 2002; *Zhao et al.*, 2003].

[1]Department of Electrical and Computer Engineering, University of Illinois, Urbana, Illinois, USA.
[2]National Center for Atmospheric Research, Boulder, Colorado, USA.
[3]Space and Environmental Technology Center, The Aerospace Corporation, Los Angeles, California, USA.
[4]Department of Physics, Clemson University, South Carolina, USA.

0148-0227/04/2002JD003056$09.00

[4] Tidal perturbations, especially the diurnal and semidiurnal tides, are very strong in the mesopause region [*Dao et al.*, 1995; *Hecht et al.*, 1998; *States and Gardner*, 2000; *She et al.*, 2002]. They can significantly influence the background temperatures and winds through which gravity waves propagate. *Liu and Hagan* [1998] used a numerical model to study the coupling between gravity waves and tides, and found that the tidal wind could strongly modify the gravity wave breaking and hence their momentum and heat fluxes. The coupling between the diurnal tide and gravity waves can also enhance the local tidal temperature amplitude to as much as 20 K. Nonmigrating tides can also result in larger than expected tidal amplitudes. These types of large perturbation was observed by *Dao et al.* [1995] and *Hecht et al.* [1998] with a sodium wind and temperature lidar during the ALOHA-93 campaign and by *Meriwether et al.* [1998] with a Rayleigh lidar located at Logan, Utah in 1995. Recently, *Williams et al.* [2002] reported an observed temperature inversion layer with a 50 K peak-to-peak amplitude oscillation between 83 and 90 km at Fort Collins with a sodium resonance lidar.

[5] In this paper, we examine the state of the atmosphere and stability properties in which the rocket was launched into in TOMEX night. We further compare the TOMEX night with three additional nights of lidar observations made afterward to identify unique and common features in the TOMEX night. The observation is also compared with TIME-GCM simulation to reveal their differences. We further examine the diurnal and semidiurnal tidal perturbations in both the observation and model simulation, to identify the tidal characteristics, and find out the extent to which the tidal perturbation is responsible for the observed unstable layers.

2. Lidar Configuration

[6] The Na wind/temperature lidar was coupled with the steerable 3.5-m astronomical telescope at SOR, Kirkland Air Force Base in Albuquerque, New Mexico. The system has been operated to make regular nighttime measurements of temperature, horizontal and vertical winds, and Na density in the mesopause region above SOR from June 1998 to November 2000. In regular operation mode, the lidar was pointed to zenith (Z), and 10° off zenith toward north (N), east (E), south (S) and west (W) in ZNEZSW sequence. The temperature, Na density and line of sight (LOS) wind profiles were obtained at every position. LOS wind at one off-zenith position can be used to derive one of the two horizontal wind components. LOS wind at zenith position gives the vertical wind.

[7] For the TOMEX night, a new operation mode was designed to measure Na density, temperature, and both components of horizontal winds in the atmospheric volume around the rocket trajectory. This new 5-position (P1–P5) mode is illustrated in Figure 1. Blue lines indicate lidar beams and the red line indicates rocket trajectory. P3 is the primary position with an elevation angle of 30.48° and azimuth of 187.02°. It intersects the upleg rocket trajectory at 95 km altitude, which is about 153 km in horizontal distance from SOR. It provides measurements of the same atmosphere volume which the rocket instruments probed. P1 and P2 have the same elevation angle as P3, but their azimuth angles are 20° away from due south (azimuth 180°) toward east and west, respectively. LOS winds measured from these two positions are used to derive two horizontal wind components. P4 has the same azimuth angle as P3, but a 10° higher elevation angle. At 95 km altitude, the horizontal distance from SOR at P4 is 107 km, 46 km closer to SOR than at P3. The measurements from P3 and P4 can provide information of meridional gradients. P5 has a slightly higher elevation angle (30.75°) than P3. The altitude difference is about 1 km near the intersection point with the rocket trajectory. The purpose is to combine the measurements from P3 and P5 to derive vertical gradients that are not contaminated by horizontal variation.

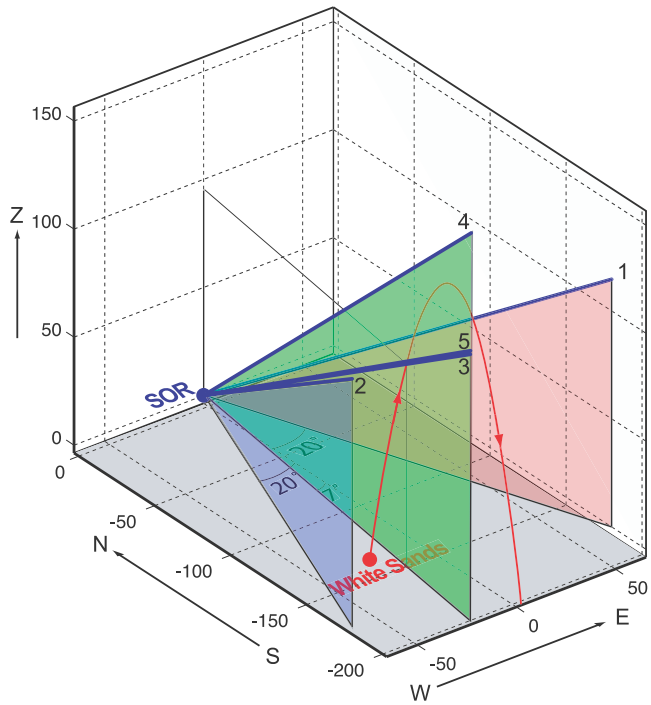

Figure 1. Configuration of TOMEX lidar operation. Blue lines indicate lidar pointing directions. Red line is rocket trajectory.

3. Data Processing

[8] During the TOMEX night, the lidar was pointed to P1 through P5 in sequence. The integration time at each position was 90 s. With additional time for moving the telescope to the next position, the temporal resolution is close to 2 min. At each position, temperature, LOS wind and Na density profiles were derived at 96 m range resolution, which corresponds to about 50 m in vertical resolution. The zonal (u) and meridional (v) winds were calculated using LOS winds from P1 and P2 as

$$u = \frac{V_1 + V_2}{2\cos 20^\circ} \tag{1}$$

$$v = \frac{V_1 - V_2}{2\sin 20^\circ}, \tag{2}$$

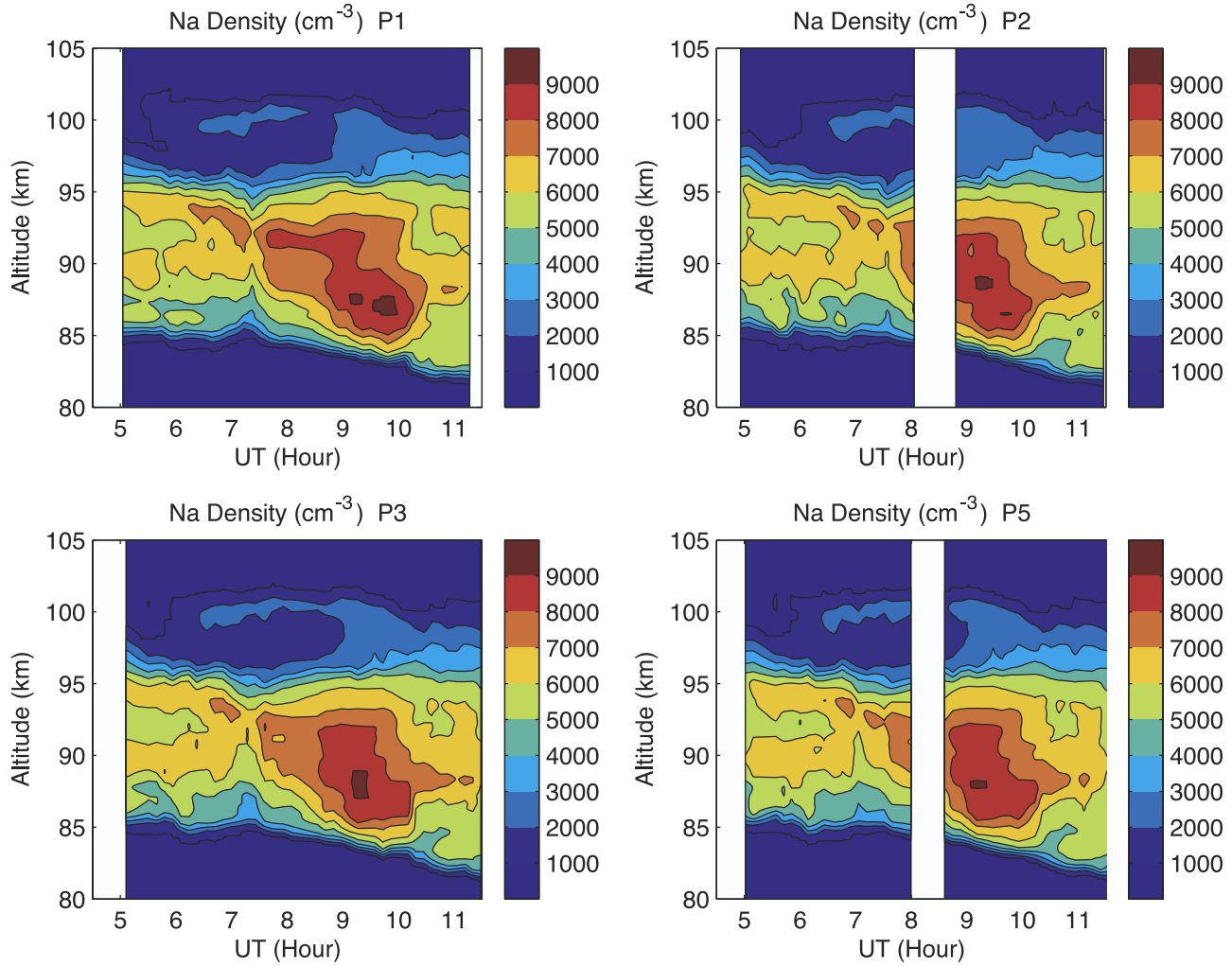

Figure 2. Na density observed at P1, P2, P3, and P5 on TOMEX night.

where V_1 and V_2 are LOS winds at P1 and P2, respectively. One pair of u and v can be derived at about every 9 min. The derived temperature, horizontal wind and Na density were then smoothed with a 1 km full-width Hamming window to further reduce noise. This is the basic data set we use for instability analysis. It covers from 0410–1134 UT (local time 10/25 21:24 to 10/26 04:34), with some gaps before 5 UT. The average uncertainties between 85 and 95 km are about 2 K, 3.5 ms^{-1}, 1.5 ms^{-1} for temperature, zonal and meridional winds, respectively. The errors increase toward the edges of the Na layer as Na density decreases. The effects of these uncertainties are considered in our instability analysis presented in section 4.2.

[9] After the TOMEX night, lidar observations were made in 3 additional nights on 27 October (0348–1108 UT), 30 October (0457–1157 UT) and 2 November (0644–1154 UT). The lidar was operated in regular mode in these nights to measure the atmosphere above SOR. These measurements were combined with that from the TOMEX night to form a 4-night average that are more representative of the mean atmospheric condition during this time of year. For this purpose, the data was binned to a lower resolution at 1 km and 30 min, and was further smoothed with 5 km and 2 hour full-width Hamming windows. At this resolution, the average errors are about 0.5 K for the temperature and 2 ms^{-1} for the horizontal wind between 85 and 95 km.

[10] Convective and dynamic stabilities are measured by buoyancy frequency and Richardson number, respectively. The buoyancy frequency N is defined as

$$N^2 = \frac{g}{T}\left(\frac{\partial T}{\partial z} + \frac{g}{C_p}\right), \tag{3}$$

where T is temperature, g is gravitational acceleration, C_p is atmospheric specific heat at constant pressure and z is altitude. The Richardson number is

$$Ri = \frac{N^2}{(\partial u/\partial z)^2 + (\partial v/\partial z)^2}. \tag{4}$$

The atmosphere is convectively unstable when $N^2 < 0$, and could be dynamically unstable when $0 < Ri < 1/4$. The vertical derivatives in these parameters were calculated for each profile, by vertical differencing with $\Delta z = 1$ km. The uncertainties of N^2 and Ri were defined by the minimum and maximum values when the temperature and wind vary by plus/minus 1-σ errors. Because the lidar was pointed at a

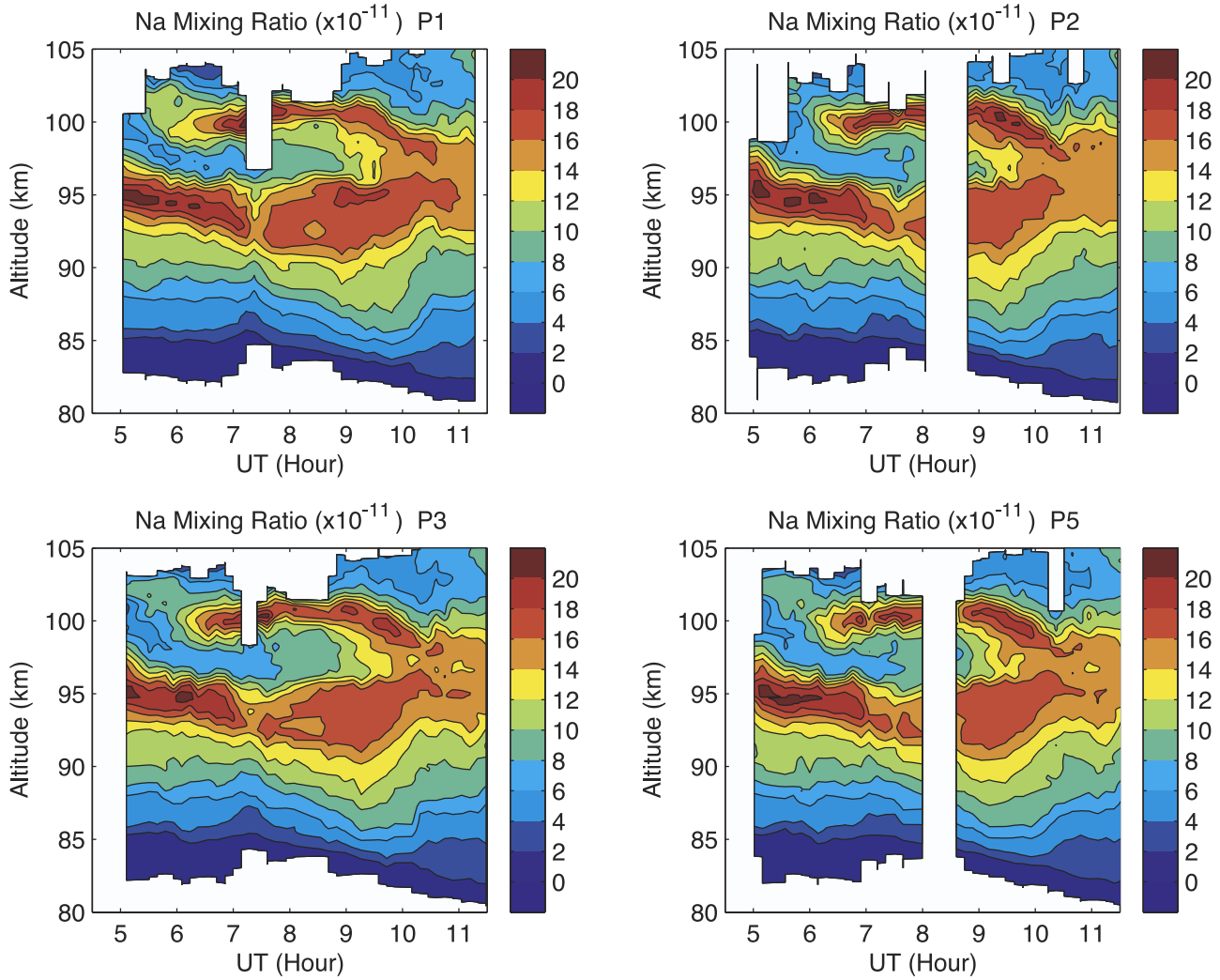

Figure 3. Same as Figure 2 but for Na mixing ratio.

slant path, the difference between two adjacent data points includes a component projected from the horizontal gradient. The effect of this was found to be negligible in the calculation of N^2 and Ri as shown in section 4.2.

4. Lidar Observations in TOMEX Night

4.1. General Features of the Atmosphere

[11] Figures 2–6 give an overview of the data obtained by the lidar over the entire evening from P1, P2, P3, and P5. They show contour plots of the Na density (Figure 2), Na mixing ratio (Figure 3), temperature (Figure 4), LOS winds (Figure 5) which are nearly meridional, and the derived zonal and meridional winds using P1 and P2 (Figure 6). Figure 7 shows line plots of Na density, Na mixing ratio, temperature, and LOS wind at 0955 UT from P5, which is the last profile taken before the launch. The focus of the discussion of these plots is on the 9 to 10 UT period.

[12] The Na density (Figure 2) shows a large peak below 90 km that occurred around 1000 UT. Above 95 km there is a large overturning feature. This can be seen more clearly with the Na mixing ratio shown in Figure 3. The Na mixing ratio is a good passive tracer for gravity wave motion above 85 km where the chemistry is less important [*Hickey and Plane*, 1995]. It was calculated the same way as in the work of *Williams et al.* [2002], where the measured temperature was used to determine the total air density based on hydrostatic relation and ideal gas law. The line plot of Na density at 0955 UT shows the overturning as a nearly altitude-independent profile between about 96 and 98 km. The Na mixing ratio shows a double peak in the same region as a result of the overturning. An additional feature in the Na density is a small-scale (a few km or less in vertical extent) structure that appears around 90 km. The overturning feature is discussed in more detail by *Larsen et al.* [2004], who identified this feature as neither a convective nor Kelvin-Helmholz instability, but rather a convective roll which is commonly seen in the lower atmosphere boundary layer region.

[13] The temperature (Figure 4) appears to be without any steep gradients prior to about 7 UT. After that time, peaking around 0930 UT a large atmospheric gravity wave or possibly a tide was present, producing a steep negative temperature gradient from 85 to almost 95 km as evidenced by the closely spaced contours. Just before the launch the minimum temperature is at around 95 km (Figure 7). The

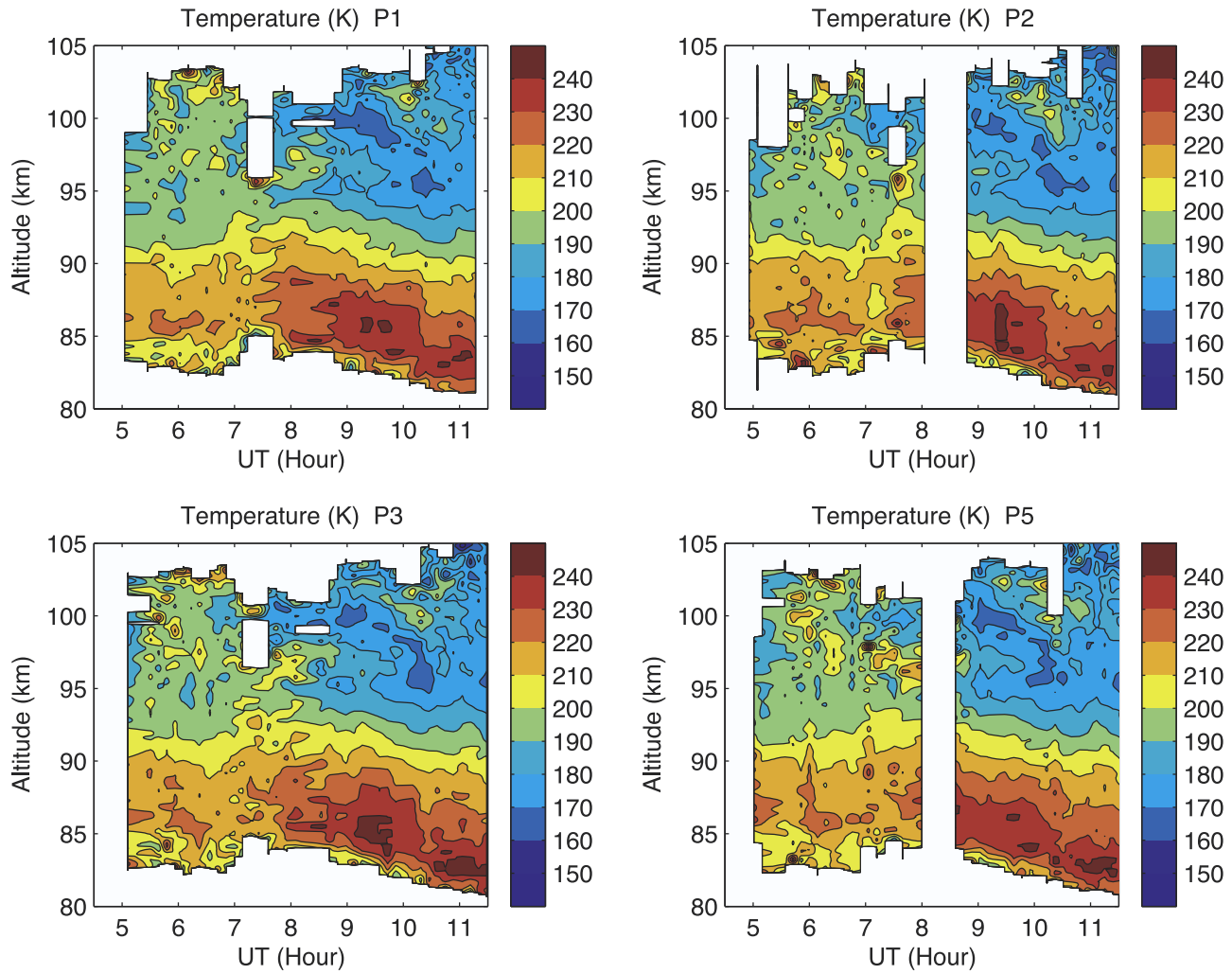

Figure 4. Same as Figure 2 but for temperature.

line plot at 0955 UT also shows some small scale structures similar to that seen in the Na at around 90 km. Additional small-scale structures can be seen between 95 and 98 km and around 85 km.

[14] The LOS winds (Figure 5) generally follow the derived meridional winds (Figure 6). Note that since the lidar was pointed toward south, the LOS winds have opposite sign to the meridional wind. There was strong northward wind at around 95 km for many hours prior to 1000 UT, and a strong shear present in the region between 95 and 100 km. That shear however was dissipating at the time of the launch. The zonal wind (Figure 6) has a shear region near 87 km for most of the hour prior to launch. There is also a zonal shear present at around 100 km.

[15] In general, the major features in these plots discussed above are similar, even though these 4 positions are spatially separated. For example, P1 and P2 are over 100 km apart at 95 km. These features thus extend horizontally over many tens to hundreds of kilometers.

4.2. Observed Unstable Regions

[16] Convective instability is likely to occur when there is large temperature gradients that exceed the adiabatic lapse rate, which is about 9.5 Kkm^{-1} in the MALT region. For the dynamic instability to occur, wind shears greater than about 40 $ms^{-1}km^{-1}$ are needed (equation (4)) since in the MALT region N^2 is about $4 \times 10^{-4}s^{-2}$ [e.g., *Hecht et al.*, 1997; *Zhao et al.*, 2003].

[17] The vertical temperature gradient and shears of horizontal wind are shown in Figure 8. They were calculated using the data from P1 and P2. The temperature gradient is based on the average temperature of P1 and P2. Just before 1000 UT, there were two regions of large shear at around 86 km, predominantly due to the zonal wind shear, and at around 96 km, predominantly due to the meridional wind shear. The latter had magnitude exceeding 40 $ms^{-1}km^{-1}$ from about 0600 UT and still had a narrow region exceeding that value just before the launch. In addition to wind shear, Ri also depends on the vertical temperature gradient. There was a large negative temperature gradient between 86 and 95 km for much of the hour before the launch. Even if this gradient was not large enough for convective instabilities, it is likely that the criterion for a dynamical instability would be exceeded since less shear is required for $Ri < 0.25$ when N^2 is small. On the opposite, in the region above 95 km the temperature gradient is sometimes positive, making a dynamical instability less likely.

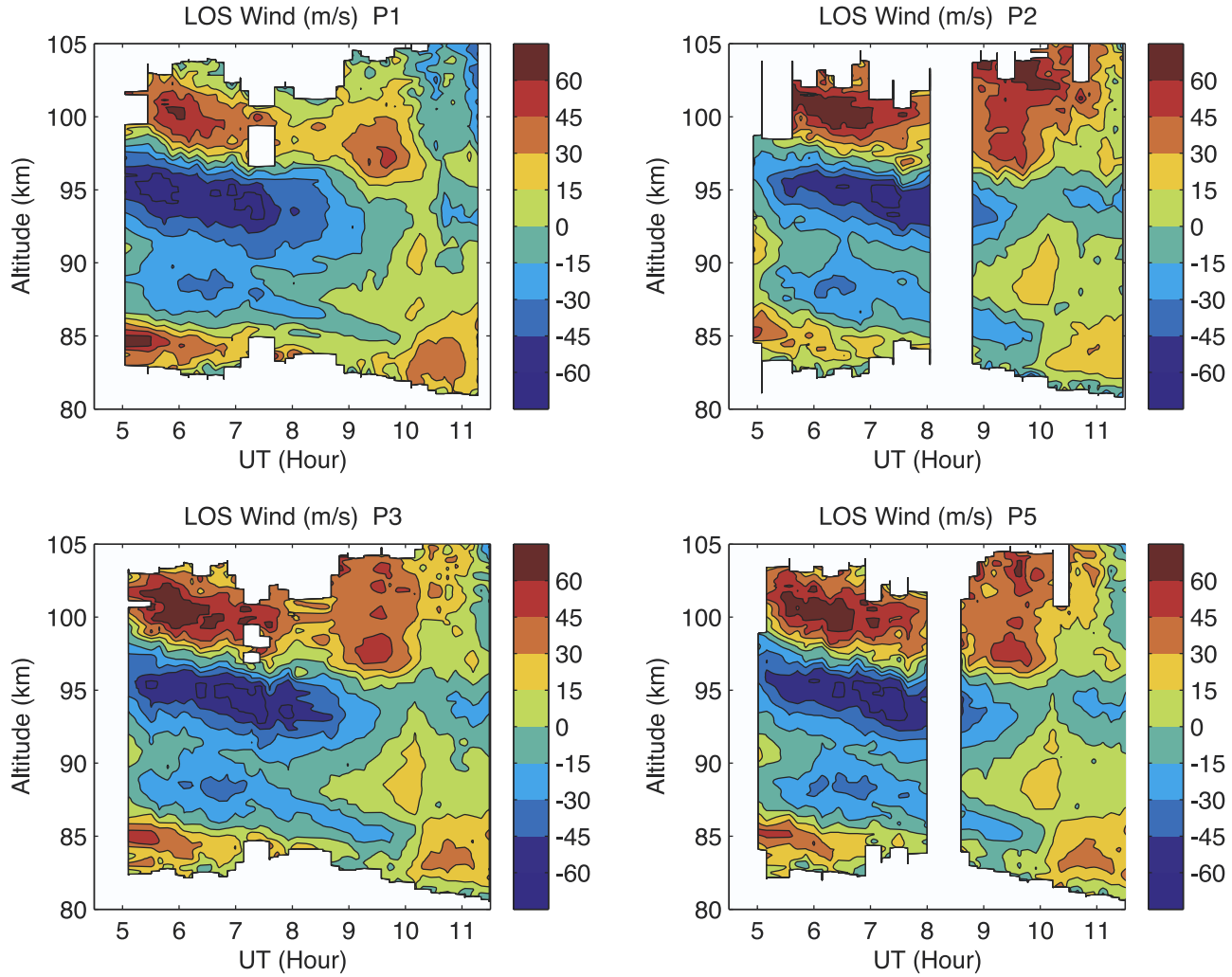

Figure 5. Same as Figure 2 but for LOS wind.

[18] The contours of convective instability parameter N^2 at 4 positions P1–P3 and P5 are shown in Figure 9. The data are shown up above 100 km although the uncertainties do increase above that altitude. All four plots show narrow regions where N^2 is less than zero between 86 and 94 km in the hour before the launch. Some also show isolated regions between 95 and 100 km where N^2 is less than zero. The unstable regions do appear to occur in narrow layers.

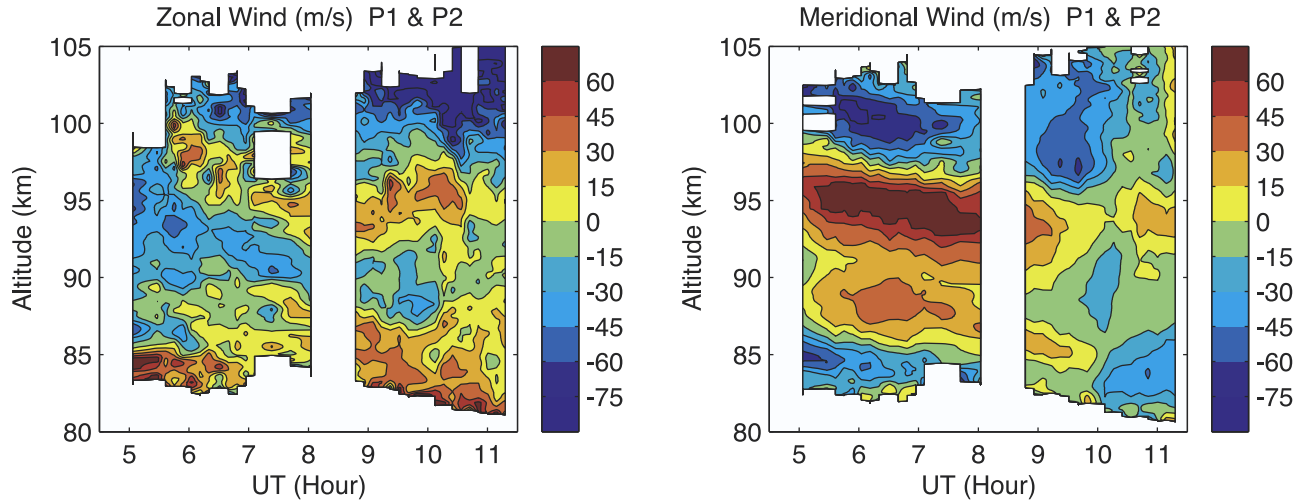

Figure 6. Zonal and meridional wind calculated from LOS wind measured at P1 and P2 on TOMEX night.

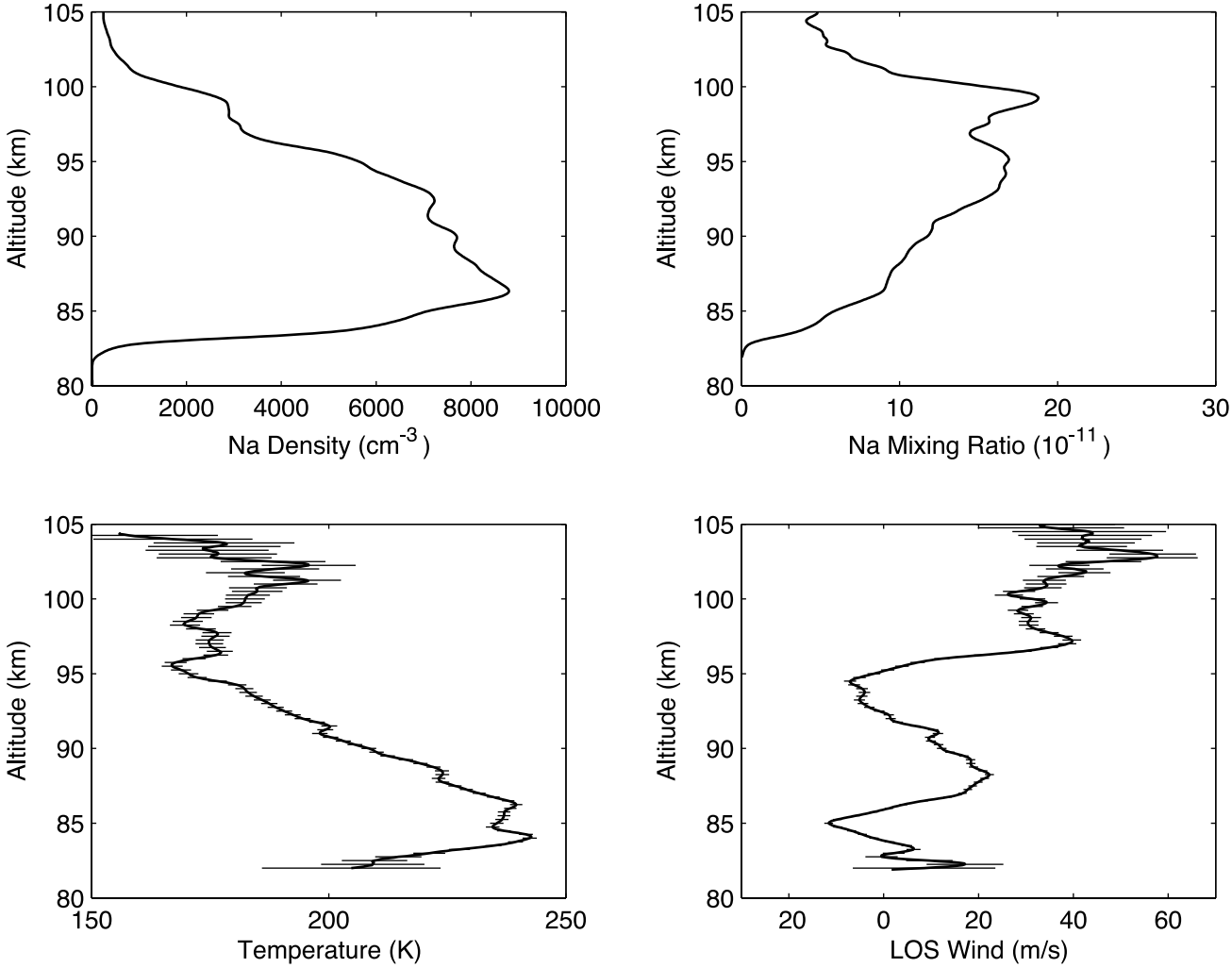

Figure 7. Na density, Na mixing ratio, temperature, and LOS wind profiles measured at P5 at 0955 UT, just before the rocket launch. Error bars for temperature and LOS wind indicate 1-σ uncertainties.

Between 9 and 10 UT almost the entire 86 to 94 km altitude range had N^2 below zero at some point in time, indicating a convective instability. The fact that all four show these potentially unstable regions suggest they are real.

[19] Each LOS measurement incorporates horizontal as well as vertical gradients. To examine the effects of horizontal gradients, we calculated the horizontal temperature gradient using temperatures from P3 and P4. It is found to be on the order of 1 to 10 K per 100 km, negligible compared with the vertical gradient. Furthermore, N^2 was also calculated using the temperature gradients obtained by vertical differencing using data from P3 and P5 which are separated vertically by about 1 km. N^2 calculated this way does not have error from horizontal gradient but does have error associated with temporal offset. The result (not shown) confirmed that much of the 86 to 94 km region had undergone a convectively unstable state at some point between 9 and 10 UT, and also indicate that at the time of the launch the region at 90 km was convectively unstable.

[20] More detailed structure of N^2 can be seen in Figure 10, which are line plots of N^2 just before and after the launch at P5. Uncertainties of N^2 from the temperature error are indicated with error bars. It clearly indicates that regions just below 90 km and 95 km have high probabilities of convective instability before launch. After launch, the unstable layer at 95 km nearly disappeared but the one at 90 km still existed.

[21] The dynamic instability parameter Ri is shown in Figure 11. It is derived by using N^2 calculated from the temperature averaged at P1 and P2 and zonal and meridional winds derived from P1 and P2. Because of this average, there are less convectively unstable regions ($Ri < 0$) in Figure 11 than in Figure 9 ($N^2 < 0$). In addition to the isolated convectively unstable regions below 95 km throughout the night, a possible convective instability also existed just above 100 km at around 1000 UT although there are considerable uncertainties in the temperatures at those altitudes. More certain is the dynamically unstable layer at 87 to 88 km which extended for over an hour beyond 10 UT, and the one at 0930 UT just above 96 km. Much earlier (prior to 0900 UT) this region had undergone dynamical instability for a period of over an hour from 6 to 7 UT.

[22] Line plots of Ri with its 1-σ error bars are shown in Figure 12 for the time just before and after the launch. The dynamically unstable layer at 87 km can be clearly identified both before and after launch with little uncertainty. The

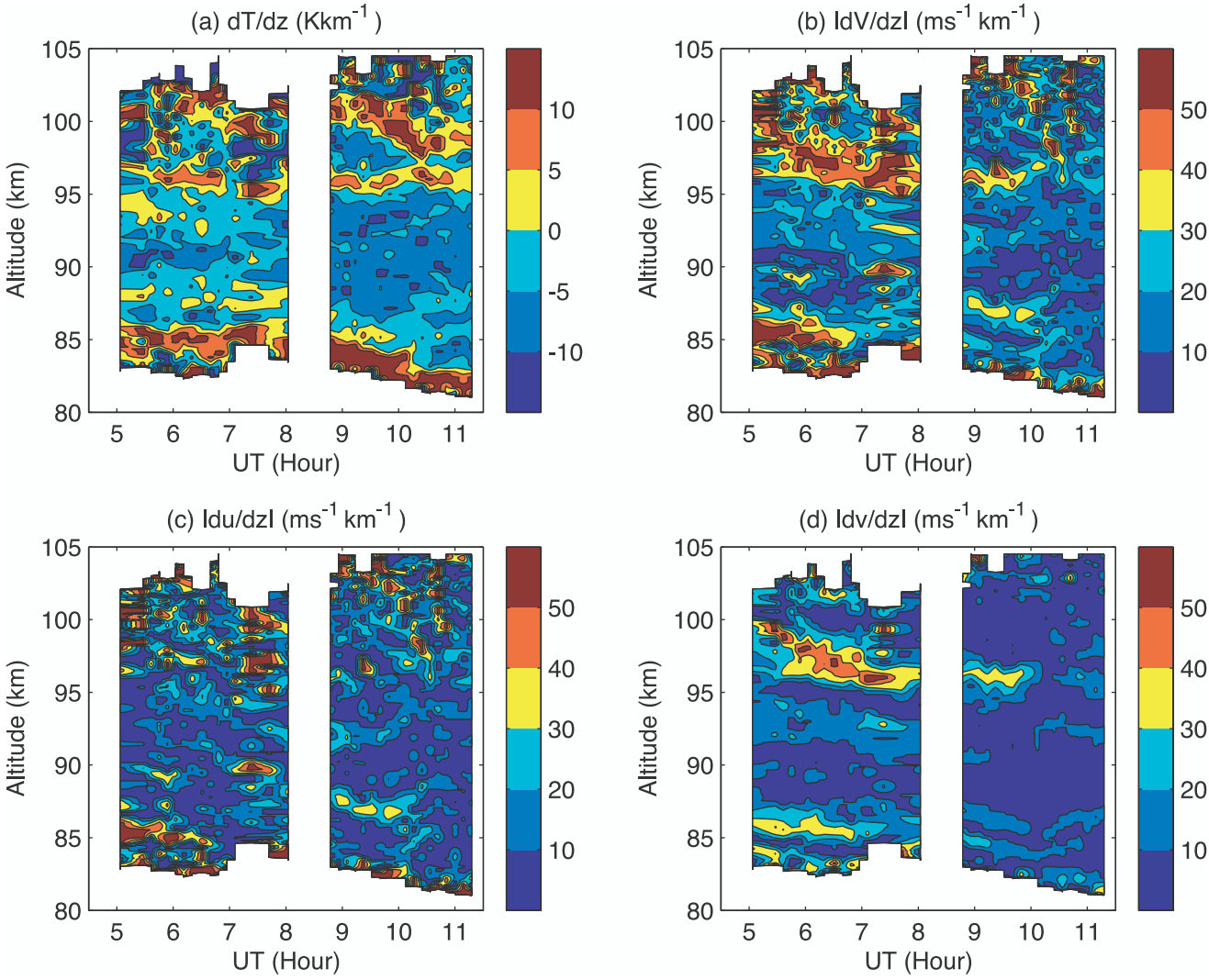

Figure 8. (a) Vertical temperature gradient, (b) total wind shear, and (c) zonal and (d) meridional wind shears in TOMEX night.

convectively unstable layer near 93 (±1) km has large uncertainty before the launch but became prominent after the launch. Note that because Ri here and N^2 in Figure 9 were based on different temperature data, $Ri < 0$ does not exactly correspond to $N^2 < 0$. Nevertheless, at around 90 and 94–95 km before launch, and at around 90, 93–94 and 102 km after launch, both parameters indicate potential convective instability.

[23] In summary, the atmosphere in MALT region during the TOMEX night have the following features. Just before launch, during the period between 9 and 10 UT, there were isolated convectively unstable layers in the region between 86 and 94 km, as well as some possible dynamically unstable layers. At 10 UT active unstable regions (probably convective, but possibly dynamic) occurred around 90 and 94 km. The region from 87 to 88 km was more or less continuously dynamically unstable from 9 to 10 UT, although convectively unstable layers appeared briefly. The region from 95 to 98 km was dynamically unstable from 6 to 8 UT and around 0930 UT. It was not unstable over a 1 km thick or larger region at the time of the launch, although it could have been at shorter scales. Above 100 km the region around 102 km may have been convectively unstable.

5. Comparison With Time-GCM Simulation and 4-Night Average

5.1. TIME-GCM Simulation

[24] The TIME-GCM is a global model of the upper atmosphere that has been described by *Roble and Ridley* [1994] with recent updates given by *Roble* [1995, 2000]. The model uses a 5 degree latitude by longitude grid with 4 grid points per scale height extending between 30 and 500 km and uses a 5 min time step. At this spatial resolution, the TIME-GCM is unable to resolve many of the small-scale features observed by the lidar and rocket. It should be able, however, to give a general tidal background upon which the small-scale gravity wave and turbulent features are superimposed. Tidal structure in the model has been analyzed by *Yee et al.* [1997], *Roble* [1995], and *Hagan and Roble* [2001].

[25] For the TOMEX simulation we use the solar radiative forcing model described by *Roble* [1995], using the

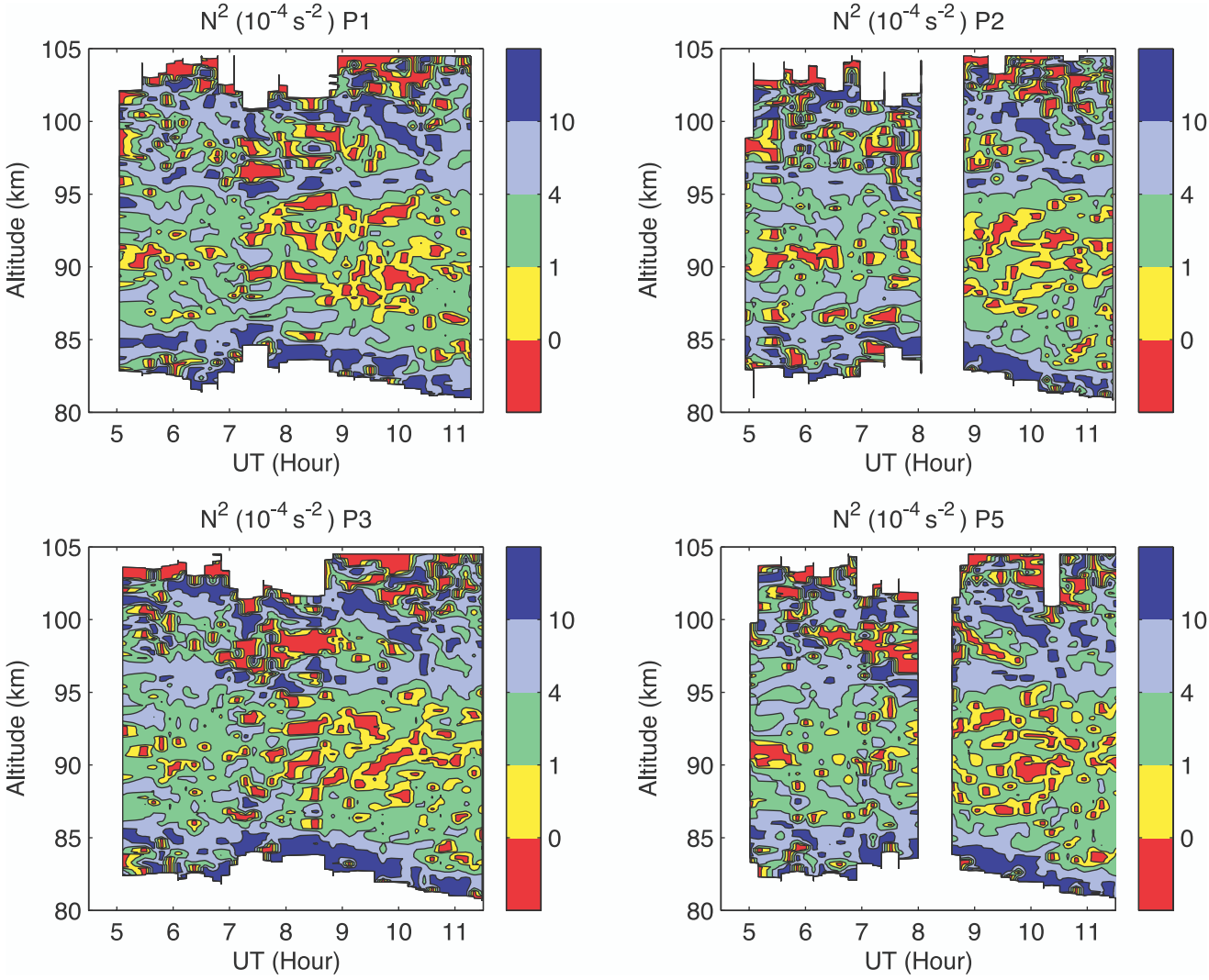

Figure 9. N^2 calculated from temperature measured at P1, P2, P3, and P5. Red regions are convectively unstable.

daily solar F10.7 variation, and with the auroral model of *Roble and Ridley* [1987] with 3 hours Kp variations driving auroral particle precipitation and the ionospheric convection cross-polar cap potential drop. At the lower boundary the NCEP geopotential height and temperature at 30 hPa are used to force the daily variation of planetary wave structure. Superimposed on the planetary wave structure at the lower boundary, which are obtained daily, are the tidal amplitudes and phases at 10 hPa specified from the Global Scale Wave Model (GSWM) of *Hagan* [1996] for the month of October. We have also run the model with the new tidal forcings that include both migrating and nonmigrating components as determined by the new study of *Hagan and Forbes* [2002] that include tidal forcings by tropospheric latent heat release. These new tidal forcings give much better agreement of the overall structure of the tidal features observed during TOMEX and they are used for comparison with data. The model also requires a specification of gravity wave forcing at the lower boundary. The gravity wave model is based on the parameterization of *Lindzen* [1981] and modified by *Kiehl et al.* [1998]. We specify a uniform 10 hPa source in latitude and longitude at the lower boundary with six waves launched in each of the cardinal directions. With these boundary conditions and specified inputs for the parameterizations all other physical and chemical processes are calculated self-consistently.

[26] This is the most realistic forcing that can be achieved for the TIME-GCM for campaign studies. The model simulation starts 10 days in advance of the TOMEX launch on 26 October 2000 and hourly histories are recorded for the day of the rocket launch for comparison.

5.2. Comparison

[27] The nightly mean temperature during the TOMEX night, over the 4-night average during TOMEX period, and from the TIME-GCM are shown in Figure 13. The temperature of the 4-night average is not far from that of the TOMEX night, indicating that the mean temperature structure is relatively stable from night to night. The TIME-GCM temperature is higher above and lower below 90 km compared with the observation, with a peak difference of about 20 K. The observed inversion layer has a peak temperature of 223 K at 86 km, while the model predicted a much weaker one (211 K) at 90 km. This is similar to the

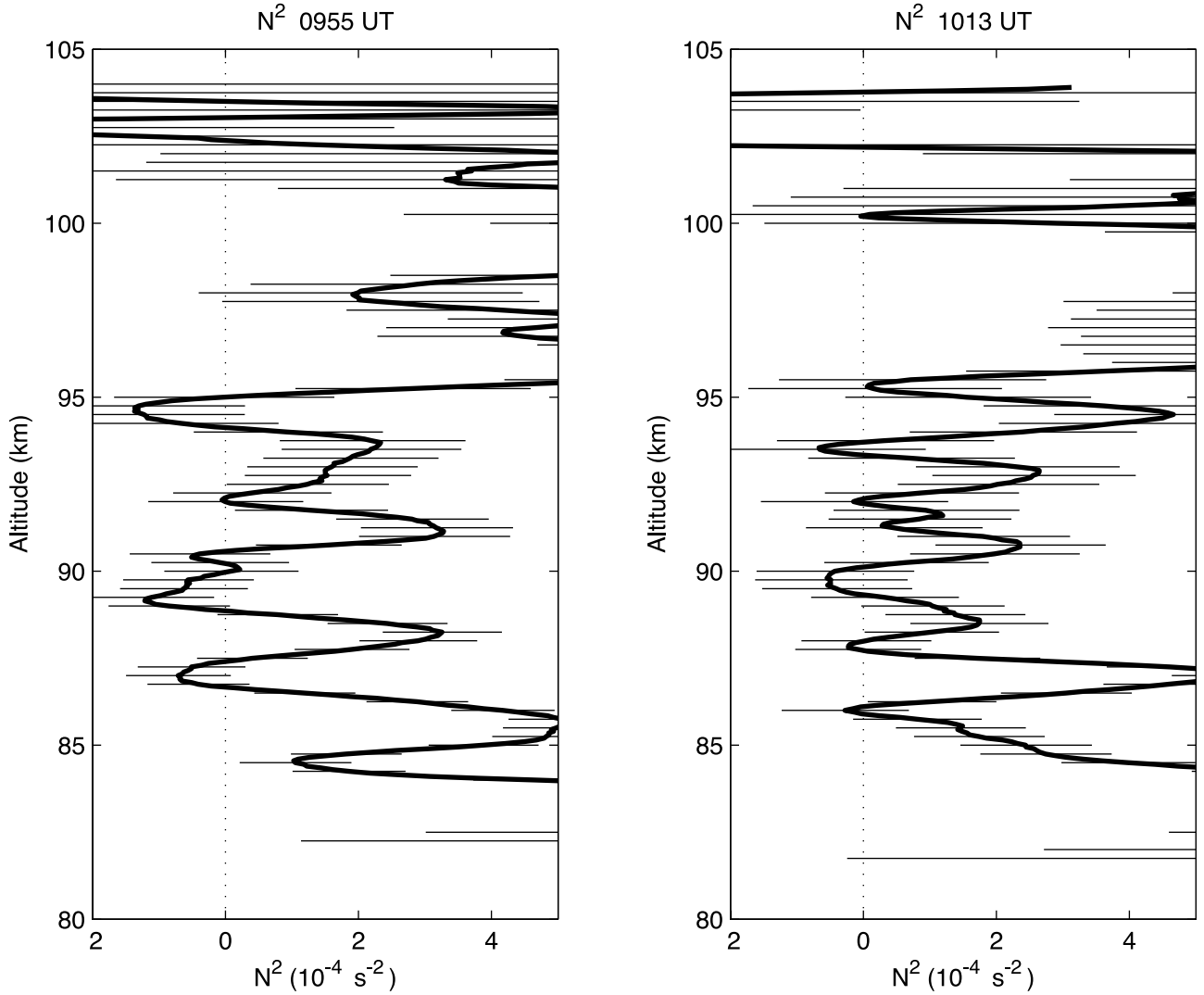

Figure 10. N^2 at P5 before and after launch. Line with $N^2 = 0$ is drawn to help identify regions of convective instability. Error bars indicate the 1-σ uncertainty.

comparison made between the lidar measurement at Haleakala (20.7°) and the TIME-GCM simulation during the ALOHA-93 campaign [*Hecht et al.*, 1998, Figure 9], where the weaker inversion layer in the model was associated with weaker predicted tidal activity.

[28] Hourly histories were recorded from the TIME-GCM for 26 October, but the results are only presented here for the time interval of the lidar measurements for comparison. Figures 14–16 show the observed temperature, zonal and meridional winds during the TOMEX night, the corresponding variables averaged over the 4-night and from the TIME-GCM simulation. The 4-night average of lidar measurements removes most day-to-day variabilities and is more representative of the tidal perturbation around TOMEX. As shown in Figure 14, the 4-night averaged temperature structure is similar to that in the TOMEX night, an indication that the large perturbation in the temperature field is mainly due to tidal perturbation. Starting at about 8 UT, the atmosphere below 90 km was quickly heated as the tides moved downward. At 95 km, the temperature decreased quickly after 8 UT. This created a large vertical

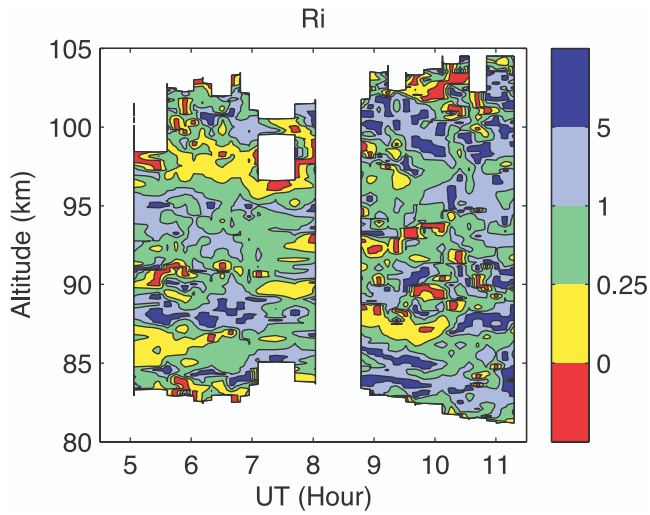

Figure 11. *Ri* calculated from temperature and horizontal wind measured at P1 and P2. Red and yellow areas are convectively and dynamically unstable, respectively.

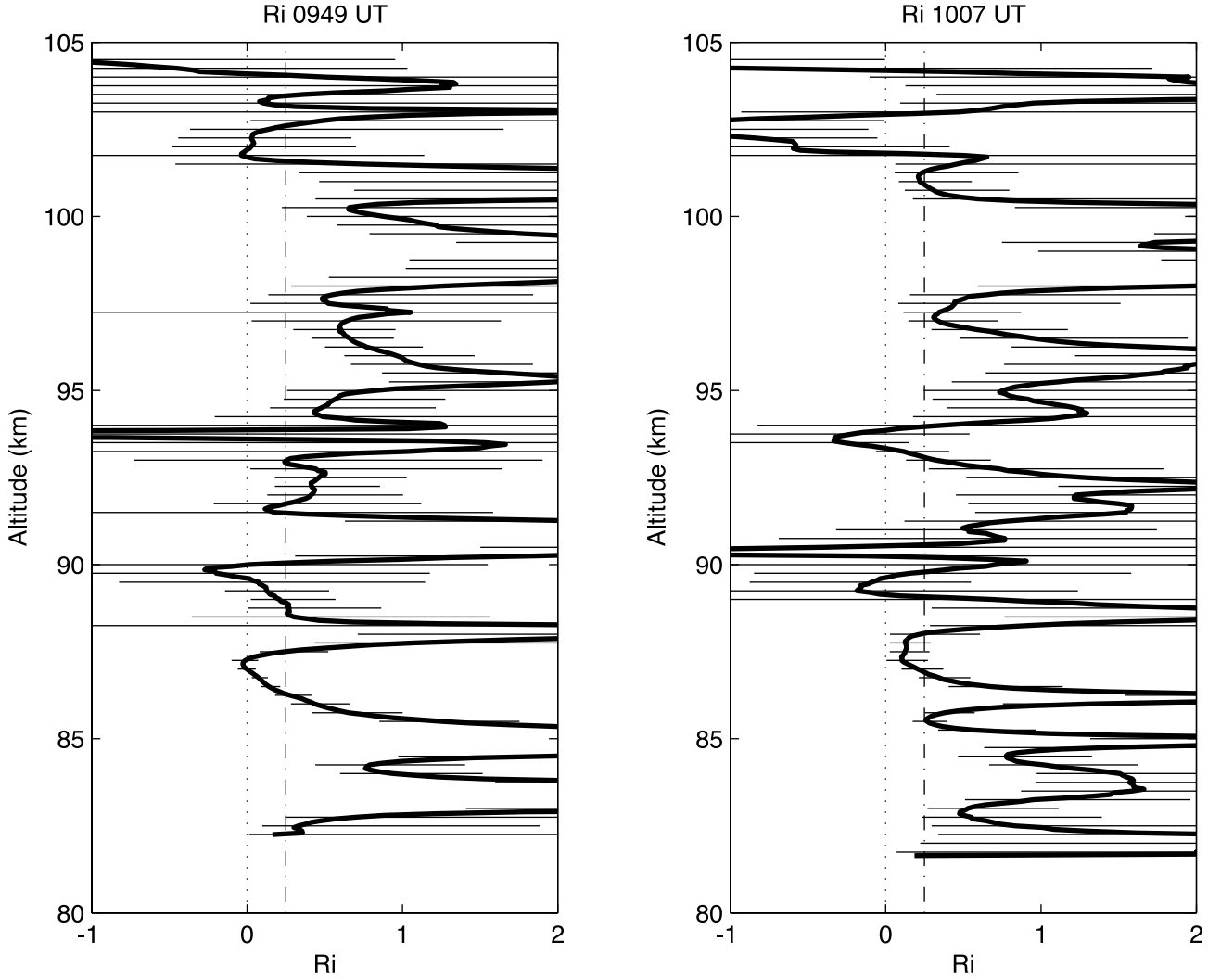

Figure 12. *Ri* before and after launch. Lines with $Ri = 0$ and $Ri = 0.25$ are drawn to help identify regions of convective and dynamical instabilities.

temperature gradient around 90 km, which led to a reduced static stability. In the TIME-GCM temperature, the height/time structure is similar to the observations, but the temperature variation is much smaller than the observed, and the peak temperature is about a couple km higher. Especially the high temperature below 90 km between 8 and 12 UT is not well captured. The peak temperature is about 20 K lower than observed.

[29] The zonal winds during the TOMEX night and over the 4-night average show some resemblance (Figure 15), with eastward winds below 90 km and westward above. The zonal wind in TOMEX night shows some tidal structure but it is not as evident as in the model simulation. The observed eastward wind moves from 100 km at 5 UT to 95 km at 9 UT, similar to the structure in model simulation. This observed zonal wind structure however shows a slower phase progress and short vertical scale, and a smaller amplitude than in the model.

[30] The meridional winds during the TOMEX night and over the 4-night average (Figure 16) have similar structures below 100 km, but with smaller peak values. The strong northward wind at around 95 km before 8 UT

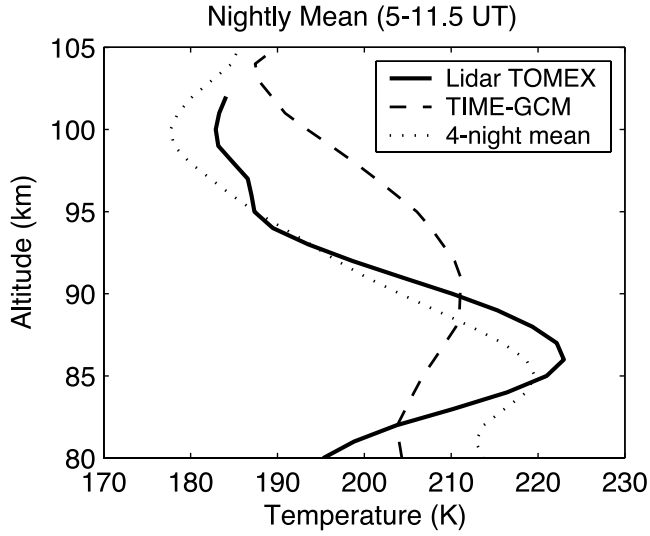

Figure 13. Nightly mean (0500–1130 UT) temperature measured by Na lidar in TOMEX night (solid line) and from 4-night average (dotted line), and simulated by TIME-GCM for the TOMEX night (dashed line).

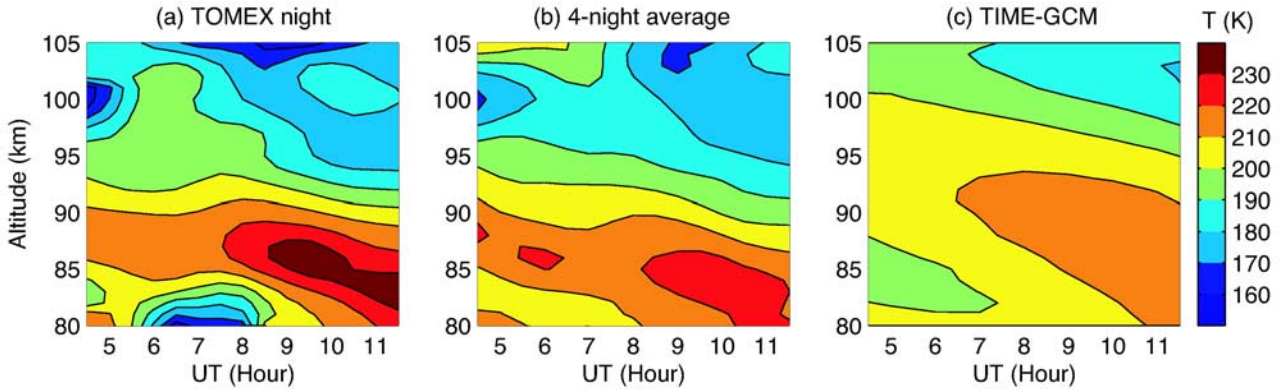

Figure 14. Temperatures (a) in TOMEX night, (b) 4-night average from lidar measurement, smoothed with 5 km and 2 hour full width Hamming windows, and (c) TIME-GCM simulation.

during the TOMEX night does not show up as strong in the averaged field. Above 100 km, the wind was southward during the TOMEX night but was northward in the 4-night average. In fact, not like the temperature and zonal wind, the meridional wind showed very strong day to day variability. For example, the meridional wind at 9 UT above 100 km was southward during the TOMEX night, but it was very weak on 27 October, and strong northward on 30 October and 2 November (not shown). The downward phase progression of the tidal activity in the TIME-GCM is in general agreement with the observed meridional wind before 9 UT, but the peak northward wind is about 2 km below the observed. While the TIME-GCM shows a mostly continuous tidal oscillation, the observations show interruptions (e.g., after 9 UT), probably due to strong wave perturbations or gravity wave breaking that occurred during the measurement period, as described by *Hecht et al.* [2004].

[31] While the model simulation shows consistent tidal perturbation in temperature and winds, the tidal signature in observation are often disrupted by various wave events. Depending on propagation directions and intrinsic characteristics, gravity wave induced perturbations in the two horizontal wind components can have different amplitudes. This make the horizontal wind field even less coherent than the temperature field.

[32] The TIME-GCM uses a steady gravity wave forcing and the calculated background stability is much greater than in the observations, indicating that the strong wave breaking, convective and shear instabilities and associated turbulence generated by the wave breaking are not properly accounted for in the model. Nevertheless, there is general overall agreement and the detailed comparison indicates that much higher resolution models are needed to model specific small-scale processes that undoubtedly have an influence on local structure.

6. Diurnal and Semidiurnal Tides

[33] To further examine the effects of tides on the convective stability during the TOMEX night, we extracted amplitude, phase, vertical wavelength and growth rate of the diurnal and semidiurnal tides in temperature by nonlinear fitting to the following function

$$T_{fit}(z,t) = A_d \exp[\beta_d(z-z_0)] \cos\left[2\pi\left(\frac{t-\phi_d}{24} + \frac{z-z_0}{\lambda_d}\right)\right] + A_s \exp[\beta_s(z-sz_0)] \cos\left[2\pi\left(\frac{t-\phi_s}{12} + \frac{z-z_0}{\lambda_s}\right)\right], \quad (5)$$

where A, λ, ϕ and β are the amplitude, vertical wavelength, phase, and vertical growth rate (inverse of scale height), respectively. z_0 = 92.5 km is a reference altitude. The subscripts d and s stand for diurnal and semidiurnal components, respectively. z is altitude and t is time in unit of hours.

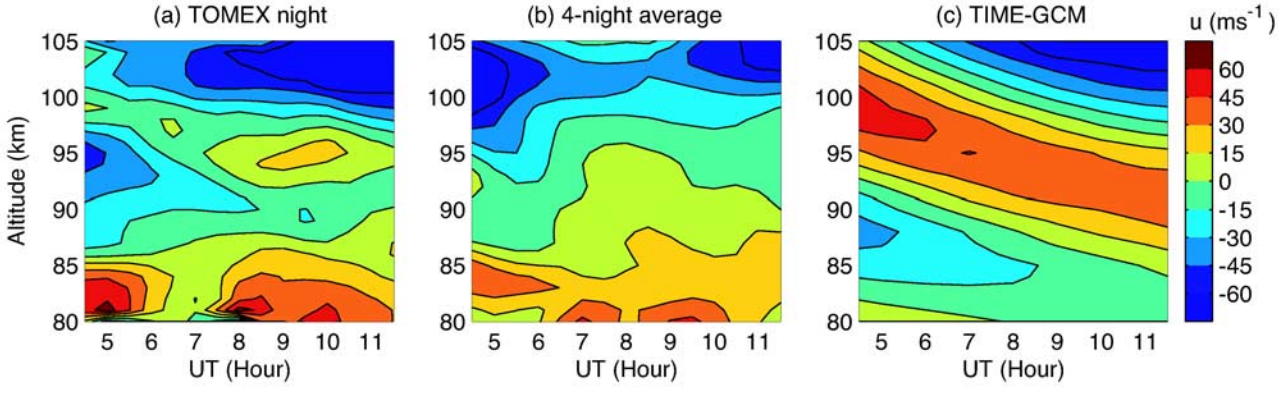

Figure 15. Same as in Figure 14 but for the zonal wind.

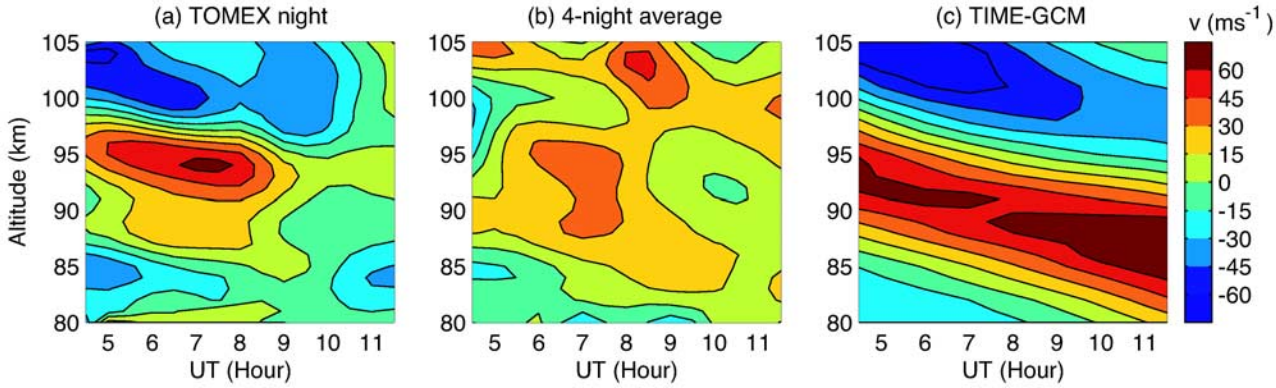

Figure 16. Same as in Figure 14 but for the meridional wind.

[34] Because there are only 6 hours of continuous lidar observation (5 UT to 11.5 UT), it is difficult to correctly fit the diurnal and semidiurnal tidal components. However, if the 24-hour mean temperature is known, it can be subtracted and the remaining temperature deviation can be fitted to the tides with good confidence if the tidal amplitudes are large. Since there was no daytime temperature measurement at SOR, the 24-hour mean temperature from the TIME-GCM was used. The 24-hour mean temperature from the TIME-GCM is reliable, because it is much easier to simulate correctly than the tidal perturbations, which have large daily variabilities, especially the nonmigrating tides. Comparisons of the TIME-GCM 24-hour mean temperature with some high latitude observations showed that their difference was well within 5 K (R. Roble, private communication). To evaluate the reliability of the fitting, we also estimated the uncertainties of the fitting parameters caused by to the uncertainty of the 24-hour mean temperature, as described below.

[35] After the 24-hour mean is subtracted, the temperature field was fitted with equation (5). The fitting function in (5) is a function of both time and altitude. The vertical wavelength and the vertical growth rate represent the vertical structure, which provide constraints to the fitting in addition to the temporal parameters. The vertical structure provides addition information and compensates for the lack of coverage in time. The fitting is therefore not very sensitive to the uncertainty of the 24-hour mean temperature. To quantify this uncertainty, we did additional fitting 500 times by varying the 24-hour mean temperature in a range of ±10 K randomly through out the altitude, and compared the fitted parameters with the original values. We defined the RMS of the difference for each parameter as the uncertainty.

6.1. Observed and Modeled Tides

[36] The amplitude, vertical wavelength, phase and growth rate of diurnal and semidiurnal temperature variation from the lidar measurements during the TOMEX night and over the 4-night average, and from the TIME-GCM simulation are shown in Table 1. For the diurnal tide, the amplitude, vertical wavelength and phase are very similar in the TOMEX night and in the 4-night average, further supporting the notion that this 24-hour component is a diurnal tide, not a low frequency gravity wave. Both growth rates are small, indicating a nearly constant amplitude with altitudes. In the model simulation, the vertical wavelength and the growth rate in the 24-hour component are in good agreement with observation, but the model amplitude is much smaller (9 K versus 26 K) and there is a 3-hour phase shift. The TIME-GCM thus produced a much weaker diurnal tide than observed. Since the large temperature perturbation due to the tides strongly affects the atmospheric stability, the weaker than observed amplitude in the model would lead to less instability and underestimate of gravity wave forcing.

[37] For the semidiurnal tides, the phase and vertical wavelength during the TOMEX night and over the 4-night average are similar but the amplitude in the 4-day average is less than half of that during the TOMEX night, and the growth rate is much larger. The model simulation gives correct phase, but longer vertical wavelength, and the amplitude is smaller (5 K versus 13 K) than the TOMEX night but similar to the 4-night average while the growth rate is similar to the TOMEX night but smaller than the 4-night average. These differences could be due to strong daily variability of the semidiurnal tide, or the existence of low-frequency gravity waves during the TOMEX night. Because the semidiurnal tide has much smaller amplitude than the diurnal tide, it is more difficult to extract the semidiurnal parameters from the data in the presence of gravity waves. Other the other hand, the effects of the semidiurnal tide on instability is also smaller.

6.2. Tidal Influence on Convective Instability

[38] The above analysis showed that there was strong tidal perturbation in temperature on the TOMEX night. The convective instability, which is associated with the vertical

Table 1. Amplitude A, Vertical Wavelength λ, Phase ϕ and Growth Rate β of Diurnal (d) and Semidiurnal (s) Tides on 26 October 2000 From Lidar Measurements and TIME-GCM Simulation and From 4-Night Average of Lidar Measurements[a]

	A_d, K	λ_d, km	ϕ_d, Hours	β_d, km^{-1}	A_s, K	λ_s, km	ϕ_s, Hours	β_s, km^{-1}
TOMEX	26 ± 2.7	25 ± 1.3	3 ± 0.4	0.008 ± 0.015	13 ± 1.4	29 ± 2.5	10 ± 0.3	0.041 ± 0.014
Four-night average	22 ± 2.4	27 ± 1.5	2 ± 0.4	0.040 ± 0.013	6 ± 1.5	25 ± 2.4	10 ± 0.5	0.145 ± 0.022
TIME-GCM	9	29	6	0.027	5	45	9	0.047

[a]Uncertainties of the fitted parameters for lidar observation due to uncertainties in the 24-hour mean temperature and measurement error are also shown.

temperature gradient, is modulated by the tides. The influence of the diurnal and semidiurnal tides on the convective instability can be examined separately. We separate the temperature field associated with tides into 24-hour mean (T_0), diurnal (T_d) and semidiurnal (T_s) components, i.e., $T^* = T_0 + T_d + T_s$. Since N^2 is a function of temperature, we can define

$$N_0^2 = N^2(T_0) \tag{6}$$

$$\Delta N_d^2 = N^2(T_0 + T_d) - N_0^2 \tag{7}$$

$$\Delta N_s^2 = N^2(T_0 + T_s) - N_0^2 \tag{8}$$

$$\Delta N_{ds}^2 = N^2(T_0 + T_d + T_s) - N_0^2, \tag{9}$$

where N_0^2 represents the 24-hour mean stability, ΔN_d^2, ΔN_s^2 and ΔN_{ds}^2 are the effects of the diurnal, semidiurnal, and diurnal plus semidiurnal tides on the stability, respectively.

[39] The mean convective stability N_0^2 is calculated using the 24-hour mean temperatures from TIME-GCM. It is shown in Figure 17. Throughout the layer, N_0^2 has an average value of 4.4×10^{-4} s^{-2}. There is a local peak of stability region at around 90 km.

[40] The effects of tides on N^2 in lidar measurements are shown in Figure 18. The main feature in Figure 18d is a low N^2 region centered around 94 km before 8 UT and then expanded and moved downward after 8 UT. At 10 UT, the minimum N^2 is 1.5×10^{-4}s^{-2}. This value is really low considering that the temperature field only includes tidal perturbation. This low stability condition set up by the tides makes instability likely to occur as waves propagating through the layer and further increasing the temperature lapse rate. The combined effects of diurnal and semidiurnal tides are shown in Figure 18a. The negative area (orange and red) is where the tides act to reduce convective stability. It coincides with the low N^2 region in Figure 18d, indicating that the low stability region in Figure 18d is a result of the tidal perturbation. Figures 18b and 18c show effects from diurnal and semidiurnal tides separately. By comparing them with Figure 18d, we can see that the low stability region is mainly due to the diurnal tide. The semidiurnal tide increased the stability before 10 UT at 94 km, opposite to the effect of diurnal tide. After 10 UT, its effect becomes negative, same as the diurnal tide. This is the time when the stability was further reduced. As discussed above, the semidiurnal tide is more susceptible to gravity wave distortion. Their effects on N^2 here may be also affected by gravity waves to some degree. Nevertheless, the data clearly show that the effects of the semidiurnal tide is small. The background variation of N^2 is mainly determined by the diurnal tide. In Figure 9, unstable layers frequently appeared between 85 and 95 km, especially after 8 UT. This is consistent with the low N^2 region in Figure 18d. The tidal perturbation however, does not capture all the unstable features. In Figure 9, the region above 95 km is unstable from 7 to 9 UT, but it does not show up in 18d, suggesting that this unstable layer may be associated with a wave disturbance with a shorter timescale.

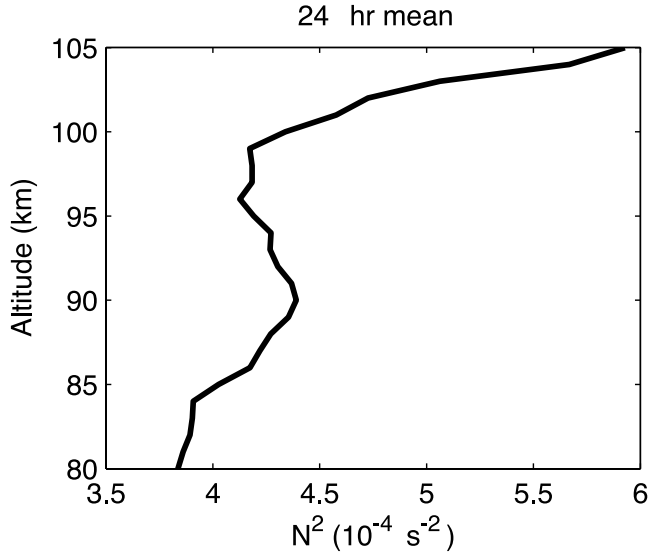

Figure 17. N^2 calculated using the 24-hour mean temperature from TIME-GCM in on 26 October 2000.

[41] The effects of tides on N^2 in the TIME-GCM simulation are shown in Figure 19. Because of the much weaker tidal amplitude in the model, the tidal effects on N^2 are also small. Figure 19d shows a similar pattern to the observation in Figure 18d but with a vertical shift of 2 to 3 kilometers. The low stability region is also mainly due to the diurnal tide. The semidiurnal tide in the model is too small to have much effect on the stability. The minimum at 10 UT in Figure 19d is 2.7×10^{-4}s^{-2}, more stable than in Figure 18d.

7. Conclusions

[42] We analyzed the convectively and dynamically unstable regions in the MALT region during TOMEX rocket campaign, based on lidar measurements of temperature and winds made on 26 October 2000 over WSMR where the rocket was launched, and 3 nights afterward over SOR, as well as the TIME-GCM simulations. Convectively unstable layers are found to occur below 95 km for extended hours before and during the launch near 10 UT. Above 95 km, there were also isolated convectively unstable regions before the launch but that region became stable at the time of launch. Large wind shears were observed at 87–88 km and around 96 km just before the launch. Dynamically unstable regions occurred at 87–88 km before launch, the lasted for over an hour. The dynamically unstable regions also appeared from 6 to 7 UT above 95 km and at 0930 UT just above 96 km. Near the launch, the potential dynamic instability associated with the strong wind shear at 96 km was suppressed due to stable temperature gradient.

[43] The lidar measurements were compared with the TIME-GCM simulation. The diurnal and semidiurnal tides were extracted from lidar observations during the TOMEX night, and over the 4-night average during the campaign, and from the TIME-GCM simulation. The model captures the overall structure of the tidal perturbation of temperature

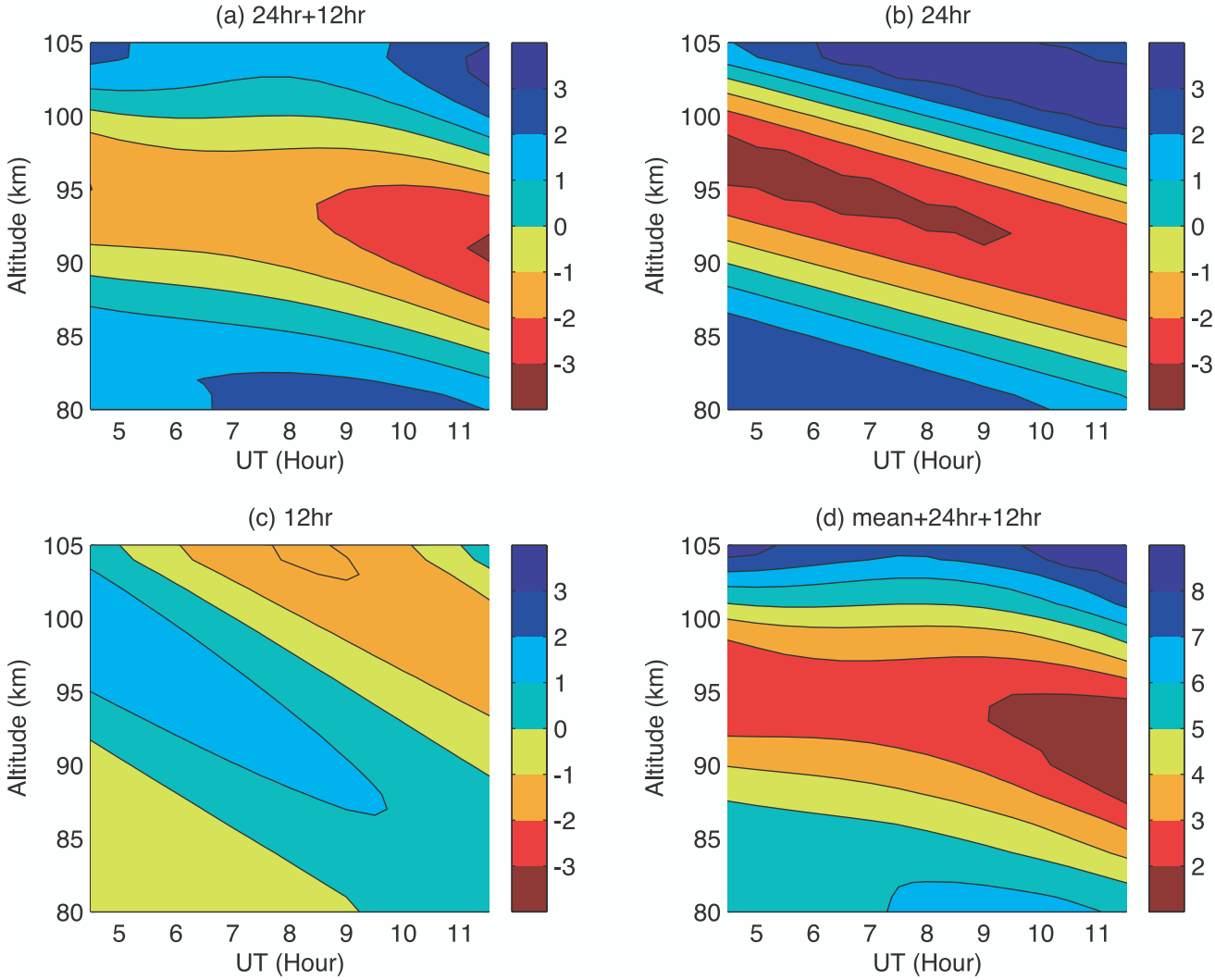

Figure 18. (a) ΔN_{ds}^2, (b) ΔN_d^2, (c) ΔN_s^2, and (d) $N^2(T_0 + T_d + T_s)$, calculated using the lidar temperature on the TOMEX night. See text for details.

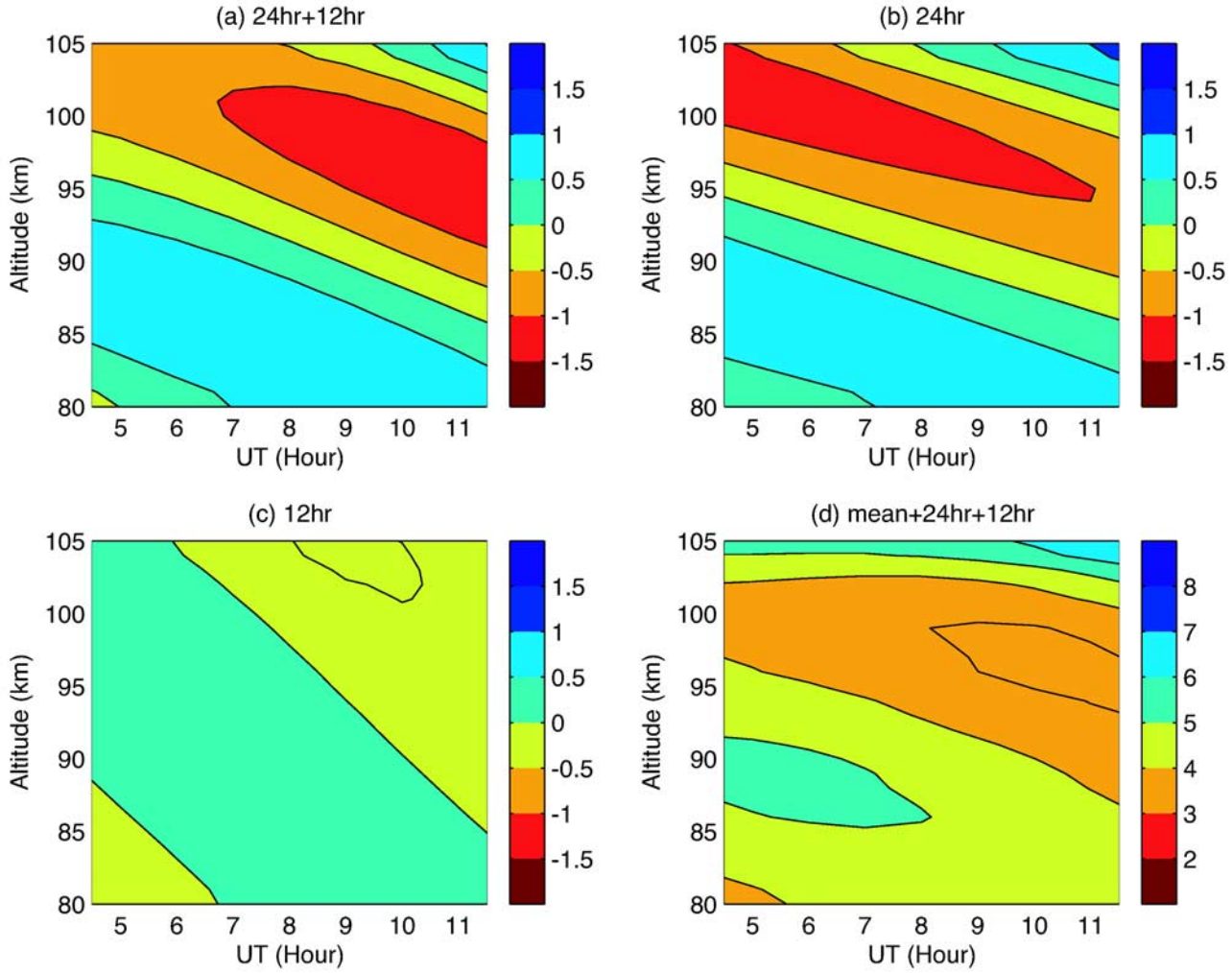

Figure 19. Same as Figure 18, but using the TIME-GCM temperature.

and horizontal wind. However, the simulated diurnal tide's amplitude in temperature is too small compared with observation: 9 K versus 26 K during TOMEX night and 22 K for the 4-night average. There is also a 3-hour phase shift in the modeled 24-hour tide of temperature. For the semidiurnal tide, the extracted tidal parameters have larger uncertainty but all indicate much smaller amplitude than the diurnal tide.

[44] The relationship between tidal perturbation and the convective stability during TOMEX was also investigated. The main feature of the stability parameter N^2 is a low stability region centered at about 94 km before 8 UT and moved downward afterward with further reduced stability. We found that this low stability region was primarily associated with the diurnal tide. The high stability region above 95 km at around 10 UT was also associated with the diurnal tide. The low stability region above 95 km between 7 and 9 UT was not induced by either the diurnal or semidiurnal tides. It may be associated with a wave disturbance with a shorter timescale.

[45] The TIME-GCM model produced temperature field that were similar in structure to the observations but with much smaller amplitudes in the tidal components. N^2 modulated by the large amplitude tides can reach very small values, making it very likely to be unstable when perturbed by gravity waves. In the TIME-GCM, the diurnal tide is much too weak to produce significant decrease in N^2. This is likely to inhibit wave breaking and dissipation, and in turn affect the gravity wave forcing calculation in the model.

[46] **Acknowledgments.** AZL and CSG acknowledge the support by NASA grant NAG 5-5241. MFL was partially supported by NASA grants NAG5-5259 and NAG5-5242 and by NSF grant ATM0003168. JHH was partially supported by NASA grant NAG5-5235, NSF grants ATM-9813834 and ATM-0122772, and by the Aerospace IR and D program. The National Center for Atmospheric Research is supported by the National Science Foundation.

References

Dao, P. D., R. Farley, X. Tao, and C. S. Gardner (1995), Lidar observations of the temperature profile between 25 and 103 km: Evidence of strong tidal perturbation, *Geophys. Res. Lett.*, *22*, 2825–2828.

Gardner, C. S., Y. Zhao, and A. Z. Liu (2002), Atmospheric stability and gravity wave dissipation in the mesopause region, *J. Atmos. Sol. Terr. Phys.*, *64*, 923–929.

Hagan, M. E. (1996), Comparative effects of migrating solar sources on tidal signatures in the middle and upper atmosphere, *J. Geophys. Res.*, *101*, 21,213–21,222.

Hagan, M. E., and J. M. Forbes (2002), Migrating and nonmigrating diurnal tides in the middle and upper atmosphere excited by tropospheric latent heat release, *J. Geophys. Res.*, *107*(D24), 4754, doi:10.1029/2001JD001236.

Hagan, M. E., and R. G. Roble (2001), Modeling diurnal tidal variability with the National Center for Atmospheric Research thermosphere-ionosphere-mesosphere-electrodynamics general circulation model, *J. Geophys. Res.*, *106*, 24,869–24,882.

Hecht, J. H., R. L. Walterscheid, D. C. Fritts, J. R. Isler, D. C. Senft, C. S. Gardner, and S. J. Franke (1997), Wave breaking signatures in OH airglow and sodium densities and temperatures: 1. Airglow imaging, Na lidar and MF radar observations, *J. Geophys. Res.*, *102*, 6655–6668.

Hecht, J. H., et al. (1998), A comparison of atmospheric tides inferred from observations at the mesopause during ALOHA-93 with the model predictions of the TIME-GCM, *J. Geophys. Res.*, *103*, 6307–6321.

Hecht, J. H., A. Z. Liu, R. L. Walterscheid, R. Roble, M. F. Larsen, and J. H. Clemmons (2004), Airglow emissions and oxygen mixing ratios from the photometer experiment on TOMEX, *J. Geophys. Res.*, *109*, D02S05, doi:10.1029/2002JD003035, in press.

Hickey, M. P., and J. M. C. Plane (1995), A chemical-dynamical model of wave-driven sodium fluctuations, *Geophys. Res. Lett.*, *22*, 2861–2864.

Kiehl, J. T., J. J. Hack, G. B. Bonan, B. A. Boville, D. L. Williamson, and P. J. Rasch (1998), The National Center for Atmospheric Research Community Climate Model: CCM3, *J. Clim.*, *11*, 1131–1149.

Larsen, M. F., A. Z. Liu, C. S. Gardner, M. C. Kelley, S. Collins, J. Friedman, and J. H. Hecht (2004), Observations of overturning in the upper mesosphere and lower thermosphere, *J. Geophys. Res.*, *109*, D02S04, doi:10.1029/2002JD003067, in press.

Lindzen, R. S. (1981), Turbulence and stress owing to gravity wave and tidal breakdown, *J. Geophys. Res.*, *86*, 9707–9714.

Liu, H.-L., and M. E. Hagan (1998), Local heating/cooling of the mesosphere due to gravity wave and tidal coupling, *Geophys. Res. Lett.*, *25*, 2941–2944.

Meriwether, J. W., X. Gao, V. B. Wickwar, T. Wilkerson, K. Beissner, S. Collins, and M. E. Hagan (1998), Observed coupling of the mesosphere inversion layer to the thermal tidal structure, *Geophys. Res. Lett.*, *25*, 1479–1482.

Roble, R. G. (1995), Energetics of the mesosphere and thermosphere, in *The Upper Mesosphere and Lower Thermosphere*: *A Review of Experiment and Theory*, *Geophys. Monogr. Ser.*, vol. 87, edited by R. M. Johnson and T. L. Killeen, pp. 1–21, AGU, Washington, D. C.

Roble, R. G. (2000), On the feasibility of developing a global atmospheric model extending from the ground to the exosphere, in *Atmospheric Science Across the Stratopause*, *Geophys. Monogr. Ser.*, vol. 123, edited by D. E. Siskind, S. D. Eckermann, and M. E. Summers, pp. 53–67, AGU, Washington, D. C.

Roble, R. G., and E. C. Ridley (1987), An auroral model for the NCAR thermospheric general circulation model (TGCM), *Ann. Geophys.*, *5*, 369–382.

Roble, R. G., and E. C. Ridley (1994), A thermosphere-ionosphere-mesosphere electo-dynamics general circulation model (TIME-GCM), *Geophys. Res. Lett.*, *21*, 417–420.

She, C. Y., S. Chen, B. P. Williams, Z. Hu, D. A. Krueger, and M. E. Hagan (2002), Tides in the mesopause region over Fort Collins, Colorado (41°N, 105°W) based on lidar temperature observations covering full diurnal cycles, *J. Geophys. Res.*, *107*(D18), 4350, doi:10.1029/2001JD001189.

States, R. J., and C. S. Gardner (2000), Thermal structure of the mesopause region (80–105 km) at 40°N latitude. Part II: Diurnal variations, *J. Atmos. Sci.*, *57*, 78–92.

Williams, B. P., M. A. White, D. A. Krueger, and C. Y. She (2002), Observation of a large amplitude wave and inversion layer leading to convective instability in the mesopause region over Fort Collins CO (41N, 105W), *Geophys. Res. Lett.*, *29*(17), 1850, doi:10.1029/2001GL014514.

Yee, J.-H., G. Crowley, R. G. Roble, W. R. Skinner, M. D. Burrage, and P. B. Hays (1997), Global simulations and observations of $O(^1S)$, $O_2(^1\Sigma)$ and OH mesospheric nightglow emissions, *J. Geophys. Res.*, *102*, 19,949–19,968.

Zhao, Y., A. Z. Liu, and C. S. Gardner (2003), Measurements of atmospheric stability in the mesopause region at Starfire Optical Range, NM, *J. Atmos. Sol. Terr. Phys.*, *65*, 219–232.

C. S. Gardner and A. Z. Liu, Department of Electrical and Computer Engineering, University of Illinois at Urbana-Champaign, 1308 West Main St., Urbana, IL 61801, USA. (cgardner@uillinois.edu; liuzr@uiuc.edu)

J. H. Hecht, Space Science Applications Laboratory, The Aerospace Corporation, M2-259, P.O. Box 92957, Los Angeles, CA 90009, USA. (james.hecht@aero.org)

M. F. Larsen, Department of Physics, Clemson University, Clemson, SC 29634, USA. (mlarsen@clemson.edu)

R. G. Roble, National Center for Atmospheric Research, Boulder, CO 80307, USA. (roble@hao.ucar.edu)